Superelastic response and damping behavior of additively manufactured Nitinol architectured materials

Yan, Zhaorui; Zhu, Jia Ning; Borisov, Evgenii; Riemslag, Ton; Scott, Sean Paul; Hermans, Marcel; Jovanova, Jovana; Popovich, Vera
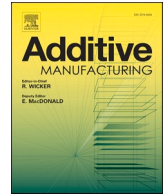
Important note
To cite this publication, please use the final published version (if applicable).
Please check the document version above.

Superelastic response and damping behavior of additively manufactured Nitinol architectured materials

Zhaorui Yan [a,*], Jia-Ning Zhu [a], Evgenii Borisov [b], Ton Riemslag [a], Sean Paul Scott [a], Marcel Hermans [a], Jovana Jovanova [a], Vera Popovich [a]

[a] *Faculty of Mechanical, Maritime and Materials, Delft University of Technology, Mekelweg 2, Delft 2628 CD, the Netherlands*
[b] *Peter the Great Saint-Petersburg Polytechnic University, Saint Petersburg, Russia*

ARTICLE INFO

ABSTRACT

In energy absorption applications, architectured metallic materials generally suffer from unrecoverable deformation as a result of local yield damage or inelastic buckling. Nitinol (NiTi) offers recoverable deformation and energy dissipation due to its unique superelasticity, which can change the way we design and additively manufacture energy-absorbing architectured materials. The interplay between microstructure, mesoscopic deformation, and macroscopic thermomechanical response of NiTi architectured materials is still not studied in depth. In this work, NiTi architectured materials featuring anisotropic superelastic response, recoverable energy absorption and damping were successfully modeled and manufactured using laser powder bed fusion (L-PBF). Extensive numerical models demonstrated that NiTi architectured materials exhibit temperature-dependent superelasticity and effective transformation stress which can be controlled by the relative density and cell architecture. An effective transformation surface was developed based on the extended Hill's model, illustrating anisotropy is temperature-independent. Stable cyclic behavior with 2.8 % of reversible strain and damping behavior was successfully achieved in cyclic compressive tests without yielding damage or plastic buckling, which further illustrates that the progressive martensitic transformation is the main deformation and energy dissipation mechanism. A comparative study between designed herein body centered cubic (BCC) and octet structures showed that local microstructures significantly affect the deformation modes. The integrated computational and experimental study enables tailoring the superelasticity by combining structural design and microstructural control. Architectured materials designed in this study are potentially applicable as reusable impact absorbers in aerospace, automotive, maritime and vibration-proof structures.

1. Introduction

Nitinol (NiTi) fabricated by additive manufacturing (AM) attracts attention due to its excellent functionalities including shape memory effect (SME) and superelasticity [1]. NiTi exhibits up to 8% recoverable strain and thermally dependent behavior due to forward and reverse martensitic transformation [2]. This adaptivity and functionality make NiTi competitive in industrial applications such as biomedical, aerospace and automotive [1,3]. For the superelastic behavior of NiTi, the austenite parent phase transforms upon loading into detwinned martensite, and transforms reversely when the load is released [4]. However, NiTi structures are conventionally manufactured by long manufacturing routes to achieve specific functionalities and shapes. Additive manufacturing, such as laser powder bed fusion (L-PBF), enables direct manufacturing of NiTi architectured materials with customized geometry and tailorable microstructure [5].

Recent developments in architectured metallic materials illustrate the successful creation of 3D lattice-based architectured materials with a high strength-weight ratio [6], tunable anisotropy [7–9], and energy absorption [10]. From the energy absorption perspective, a bending-dominated structure shows long plateau stress, whereas stress oscillates layer-by-layer in stretching-dominated structures [11]. However, such structures generally absorb energy through plastic deformation, which implies they are not sustainable after use. For shock protection, the loading event can impart multiple loading, so recoverability of deformation in energy dissipation application is needed [12]. Here, a combination of superelastic NiTi and architectured materials provides a feasible solution to design and additively manufacture
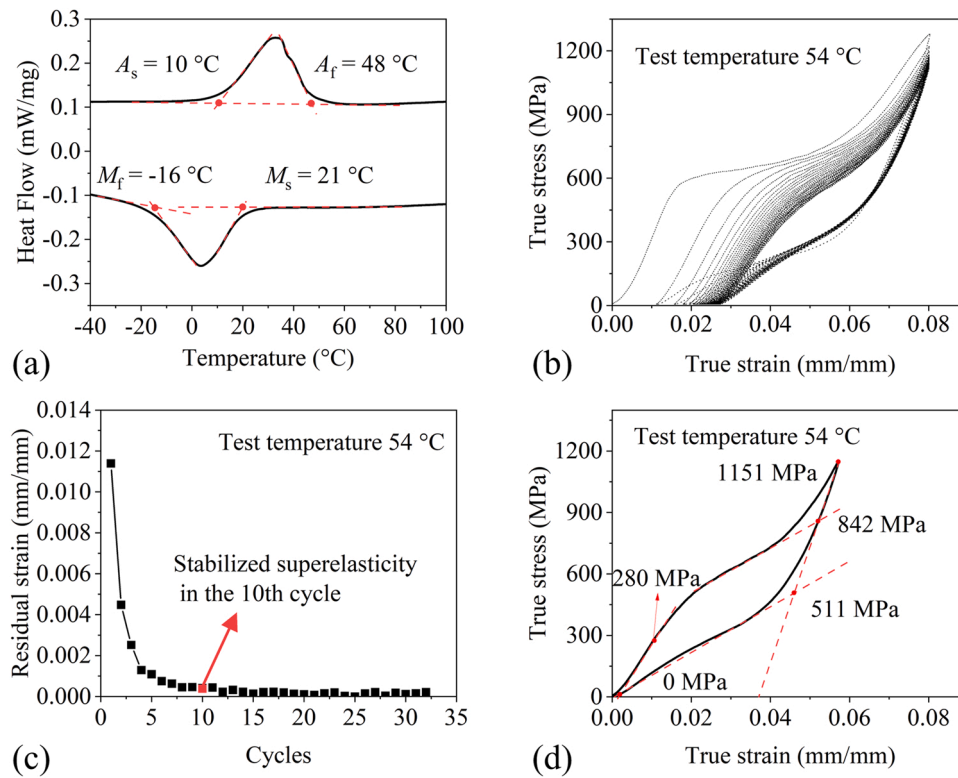
Fig. 1. Thermomechanical properties of NiTi bulk material: (a) DSC curve, (b) cyclic compression, (c) stabilization in the 10th cycle, (d) and transformation stress.

reusable energy-absorbing architectured material. Due to the nature of dissipative energy in damping behavior, cyclic energy dissipation can be formulated as damping. Golovin and co-workers attributed high damping capacity in stochastic cellular material to stress hysteresis caused by local yielding behavior, but this damping property can result in crack initiation and early failure [13,14]. For NiTi architectured materials, the damping behavior can be considered as a martensitic transformation loss factor, and the underlying mesoscale deformation of the transformation damping needs to be clearly illustrated.

Building on early works [15,16], extensive analytical and computational studies have explored the designed parameter space by relating the nonlinear response of different cell architectures and external loading conditions [11,17,18]. Numerical studies have focused on understanding the complex relations between elastoplastic constituent materials and different architectures [17,19–22]. To simulate the macroscopic response of NiTi architectured materials, some studies simplify NiTi as an elastoplastic constituent material [23,24]. Ravari et al. [25] investigated the macroscopic stress response of the NiTi body centered cubic (BCC) lattice and experimentally validated it. Viet et al. [26] developed the effective response of the NiTi primitive unit cell model based on the Zaki and Moumni model [27]. However, the interplay between NiTi constitutive model and macroscopic thermomechanical response is not clearly discussed. Due to the temperature-dependent functionalities of NiTi, rescaling of properties-density relations is crucial for discovering new design paradigms and tailorable functionalities.

The fast development in the L-PBF of NiTi provides controllable process parameters allowing to mitigate macroscopic defects and tailor its functional properties. The successful additive manufacturing of NiTi samples demands careful optimization of process parameters and choice of raw powder [28–31]. NiTi structures with complicated shapes were successfully manufactured based on parametric studies on bulk material [32–35]. Several works explore the manufacturing parameters for NiTi 2D honeycomb [23], micro-lattice [36] and micro stent with a one-way shape memory effect using an equiatomic raw powder. Saedi et al. [37]

fabricated porous NiTi material with superelasticity achieved using heat treatments. Yang et al. [38] investigated the effect of volume fraction on the compressive behavior of NiTi Gyroid structures. However, for cyclic loading conditions, cyclic stability and immediate recovery without external stimulus are required. Achieving stabilized superelasticity in architectured materials directly from the L-PBF process is still challenging. The influence of microstructure on the functional properties of NiTi lattices is widely neglected and mechanical properties of polycrystalline NiTi are simplified as phenomenological models in numerical simulation [4,39]. To the best of our knowledge, most of the current research is focused on process optimization and functionality in AM process. The relation between L-PBF NiTi microstructure, mesoscopic deformation modes and the macroscopic thermomechanical response has not been dealt with in depth. Therefore, a comprehensive study, which combines phenomenological modeling, microstructure characterization and experimentally validated stabilized superelastic behavior is needed.

This work aims to explore the superelastic response space and damping properties of NiTi architectured materials. BCC and octet structures are chosen to represent respective deformation modes. The macroscopic superelastic response of both structures is modeled and compared, with consideration of anisotropy and temperature dependence. An effective initial transformation surface with temperature loading is developed based on the extended Hill's model. Simulations are validated under quasi-static compressive loading using Ni-rich NiTi bulk and lattice samples fabricated using L-PBF. Recoverable energy absorption and damping properties are obtained after stabilization in cyclic compression tests. Comparative studies between bulk, bending-dominated and stretching-dominated structures are conducted to show the consistency and deviation of composition, microstructure and local superelasticity. The competitive influence between mesoscopic deformation modes and microstructure on macroscopic superelasticity and energy absorption capacity is discussed.

Table 1

Summary of thermomechanical experimental results used for calibration of NiTi constitutive relations.

Thermomechanical properties	Unit	Value
Austenite Young's modulus (E_A)	GPa	32.584
Austenite Poisson ratio (ν_A)	-	0.33
Martensite Young's modulus (E_M)	GPa	56.592
Martensite Poisson ratio (ν_M)	-	0.33
Transformation strain (ε_t)	-	0.37
Martensite start stress (σ_{Ms})	MPa	280
Martensite finish stress (σ_{Mf})	MPa	842
Austenite start stress (σ_{As})	MPa	511
Austenite finish stress (σ_{Af})	MPa	0
Clausius–Clapeyron relation (C_{AS}, C_{SA}) [45]	MPa/°C	6.5
Reference temperature (T)	°C	54
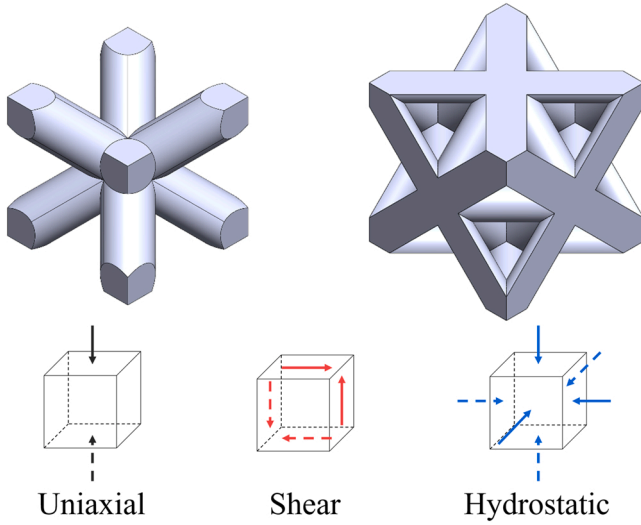
Fig. 2. RVEs with a relative density of 0.4 and loading conditions.

Fig. 3. (a) Definition of macroscopic planes on BCC and octet structures, (b) CAD coordinate for L-PBF coordinate system and scanning strategy and (c) as-fabricated samples.

2. Design and finite element modeling

2.1. Relative density

To explore the superelastic response of lattice-based architectured materials, body centered cubic (BCC) structures and octet structures are chosen as the architecture cases to represent bending- and stretching-dominated modes along the < 100 > loading direction [40]. The macroscale mechanical properties of both structures vary with relative density, which is defined by the ratio of their density to the density of the base material. For a latticed-based structure composed of solid beams [11,17], the relative density $\bar{\rho}$ can be given by the second-order approximate equation

$$\bar{\rho} = C_1 \left(\frac{R}{l}\right)^2 - C_2 \left(\frac{R}{l}\right)^3, \qquad (1)$$

where R and l are the radius and length of the beam. C_1 and C_2 are structure-dependent constants, which are $3\sqrt{3}\pi$ and $18\sqrt{2}\pi$ for a BCC structure, and $6\sqrt{2}\pi$ and 54.6 for an octet structure.

2.2. Constitutive material model

The superelastic behavior of NiTi is modeled based on the phenomenological model developed by Auricchio et al. [41]. Austenite and Martensite are assumed to follow isotropic linear elasticity. The stress-induced forward and reverse phase transformation surfaces are modeled using the Drucker-Prager loading surface
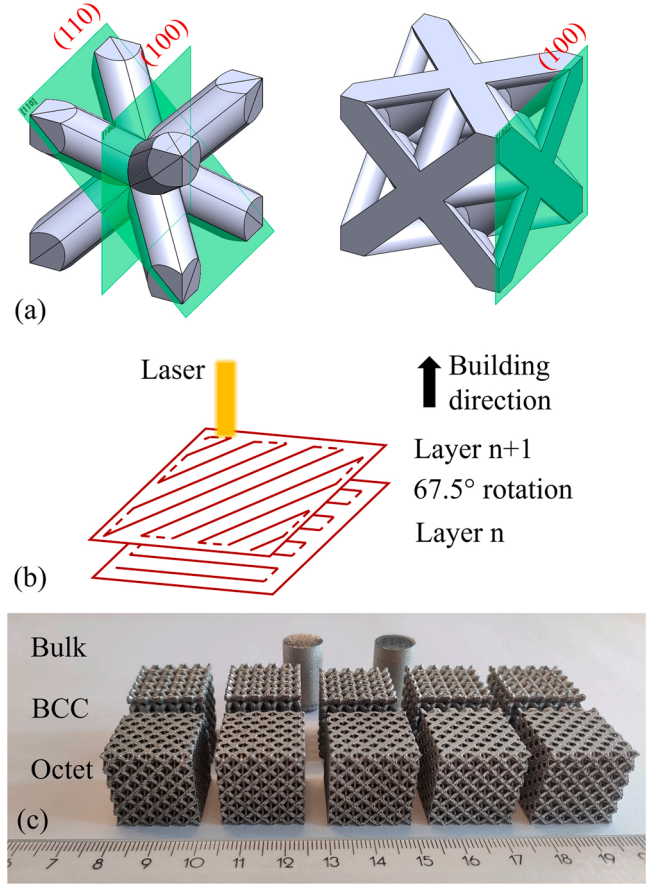
Table 2

L-PBF process parameters used in this study.

Laser power (W)	Scanning speed (mm/s)	Hatch distance (mm)	Layer thickness (mm)	Volume energy density (J/mm³)
400	1250	0.120	0.030	88.9

$$F_{AS}(\sigma, T) = \|\sigma_{dev}\| + 3\alpha p - C_{AS}T, \qquad (2)$$

where σ_{dev} is the deviatoric part of the stress, p is the pressure, and α is a material parameter. The transformation surface is linearly dependent on temperature T, which is described by Clausius–Clapeyron relation

$$C_{AS} = C_{SA} = \frac{d\sigma_{tr}}{dT} = \frac{\Delta S}{\varepsilon_{tr}}, \qquad (3)$$

where C_{AS} and C_{SA} are coefficients defined as the slopes of the stress-temperature boundaries for forward and reverse transformations respectively. σ_{tr} is the transformation stress, ΔS is the entropy variation and ε_{tr} is the transformation strain. Transformation-induced plasticity is neglected and martensite fraction ξ is the internal variable used to describe the evolution of transformation strain in the flow rule.

2.3. Characterization of material properties

NiTi thermomechanical properties need to be carefully calibrated for the phenomenological material model because NiTi exhibits functional degradation during the cyclic loading test. In order to mitigate the
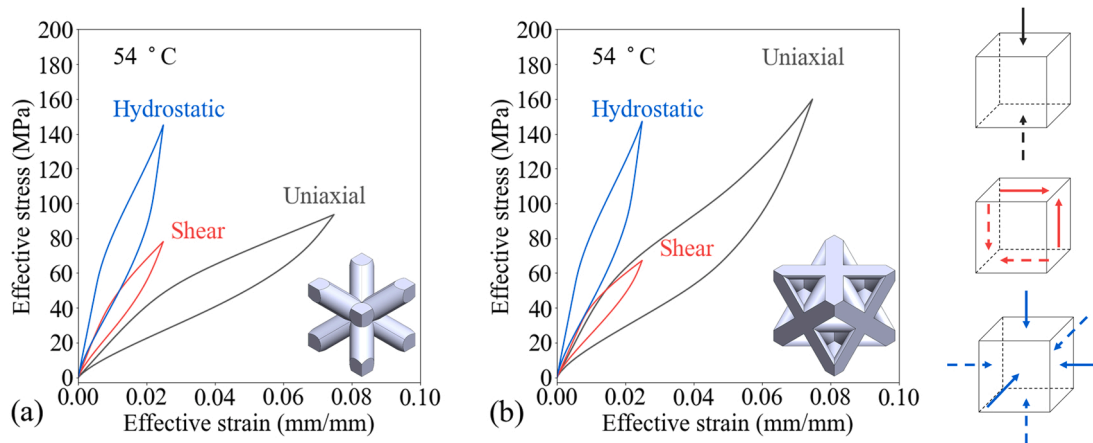
Fig. 4. Effective stress and strain diagrams of (a) BCC and (b) octet RVEs for uniaxial, shear and hydrostatic loadings at 54 °C.
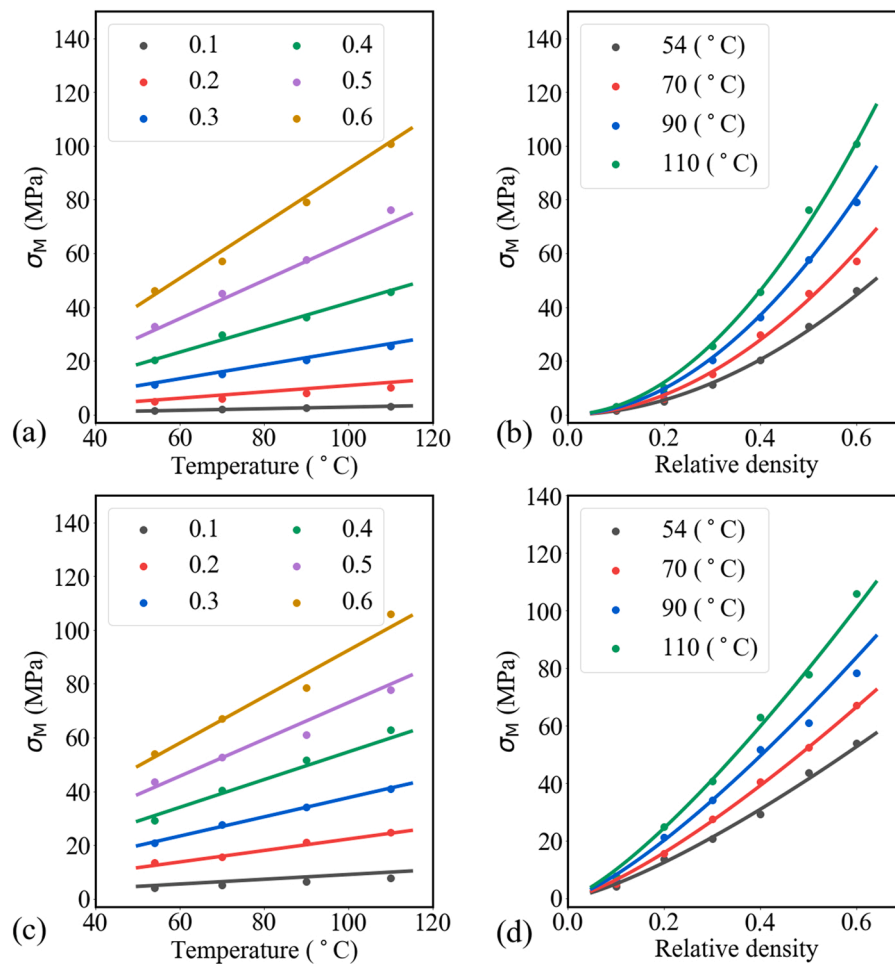

Fig. 5. Effect of temperature loadings and relative densities on martensite start stress under uniaxial loading of (a)(b) BCC and (c)(d) octet RVEs.

statistical deviation of thermomechanical properties resulting from different cycles, the material properties were calibrated from the cyclic compression tests on bulk samples. Calibration methods are introduced in Section 3 in detail. To determine the temperature required for subsequent mechanical testing, transformation temperatures (TTs) were measured from the differential scanning calorimetry (DSC) curves as shown in Fig. 1(a). The testing temperature for uniaxial compression was determined to be 6 °C higher than the austenite finish temperature A_f, which ensures a fully austenitized parent phase. Cyclic compression

tests were conducted until superelasticity was completely stabilized (Fig. 1(b)). As can be seen, the superelastic response of bulk material can be stabilized after 10 cycles with the residual strain lower than 0.038 % (Fig. 1(c)) [42]. In the 10th cycle, the statistical deviation of mechanical properties under 54 °C is negligible, and the main mechanical properties of additively manufactured NiTi bulk samples are calibrated in the 10th cycle of cyclic compression tests (Fig. 1(d) and Table 1). Young's modulus of austenite and martensite is determined using the tangent line. The initial transformation stress is measured using the parallel line

Table 3

Power-law parameters for transformation stress of BCC and octet structures.

	k_1	p_1	k_2	p_2
BBC				
Uniaxial	0.424	1.92	0.426	1.96
Shear	0.178	1.23	0.157	1.21
Hydrostatic	0.563	1.25	0.519	1.22
Octet				
Uniaxial	0.368	1.31	0.254	1.27
Shear	0.351	1.34	0.270	1.29
Hydrostatic	0.654	1.30	0.530	1.17

Table 4

Dimensions and density of as-designed compared with L-PBFed samples.

Architectured materials	Strut diameter (mm)	Volume (mm³)	Mass (g)	Relative density (-)
As-designed BCC	1.30	8000.00	20.6	0.4
As-fabricated BCC	1.67 ± 0.08	7910.67 ± 22.02	24.8 ± 0.9	0.486 ± 0.021
As-designed octet	0.84	8000.00	20.6	0.4
As-fabricated octet	1.11 ± 0.06	7982.41 ± 8.97	25.4 ± 0.2	0.494 ± 0.004

Table 5

EDS compositional analysis of different NiTi structures.

Samples	Ni (at. %)	Ti (at. %)
Powder	50.60 ± 0.10	49.40 ± 0.10
Bulk	50.30 ± 0.15	49.70 ± 0.15
BCC	50.20 ± 0.10	49.80 ± 0.10
Octet	50.20 ± 0.15	49.80 ± 0.15

Table 6

Martensitic transformation temperature (°C) of different structures (obtained by DSC).

Sample	A_s	A_f	M_s	M_f
Bulk	10	48	21	-16
BCC	-19	53	27	-42
Octet	4	69	38	-19
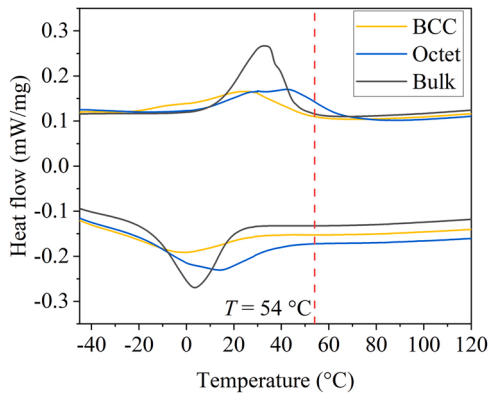
Fig. 6. DSC curves for bulk, BCC and octet samples.

at the strain of 0.2 %. The low Young's modulus of austenite likely resulted from either R-phase transformation, or a strong [001] texture parallel to BD and residual martensite generated in the L-PBF process and cyclic compression [43,44].

2.4. Unit cell model and effective martensitic transformation

The effective superelastic behavior of representative volume element (RVE) is predicted using a unit cell model with periodic boundary conditions (PBC). Applying PBC on structures with nonlinear material behavior was discussed in earlier research [46]. The unit cell model is discretized using first order block elements (C3D8R) to ensure symmetric meshes on the paired surfaces. The displacement of nodes on the paired surfaces is coupled with the displacement of dummy nodes using constraint equations [47]. Nodes located on the edges and vertices are also considered in constraint equations excluding redundant equations. The displacement components of nodes in PBC are formulated as

$$u_i^{j+}(x,y,z) - u_i^{j-}(x,y,z) = c_i^j \qquad (i,j = 1,2,3), \tag{4}$$

where $j+$ and $j-$ denote the positive and negative normal of paired surfaces, and i is the displacement component in Cartesian coordinates.

Simulations for BCC and octet RVEs with a unit cell size of 4 mm and a relative density ranging from 0.1 to 0.6 are performed to understand the density-properties relation. Three displacement loading conditions are applied to dummy points of the RVEs to simulate superelastic behaviors in a stabilized cycle as shown in Fig. 2. Uniaxial compression is applied along the [100] direction with the maximum displacement of 0.3 mm to simulate the uniaxial transformation stress. Pure shear with a maximum displacement of 0.1 mm is applied along 1–2 plane and 2–1 plane to simulate the shear response: $\mathbf{F} = \mathbf{1} + \varepsilon_{\max}(\mathbf{e}_1 \otimes \mathbf{e}_2 + \mathbf{e}_2 \otimes \mathbf{e}_1)$. Hydrostatic compression with a maximum displacement of 0.1 mm is applied in three normal directions. Constant temperature loading $T = $ (54, 70, 90 and 110) °C is applied on all RVEs to simulate the effect of temperature T on transformation stress.

After the numerical solution of the RVEs, the effective stress of RVEs is obtained by the reaction forces $\mathbf{RF}$ on the 3 dummy nodes and the unit cell size L:

$$\bar{\sigma}_{ij} = \frac{\mathbf{e}_i \cdot \mathbf{RF}_j}{L^2} \tag{5}$$

The effective martensite fraction $\bar{\xi}$ is determined by the volumetric average of the martensite fraction over the whole RVE:

$$\bar{\xi} = \frac{1}{V}\int_V \xi \mathrm{d}V, \tag{6}$$

where V is the volume of the RVE.

2.5. Uniaxial compression simulation

The uniaxial compression response of both structures with $5 \times 5 \times 5$ cells tessellation is modeled to simulate the stabilized cycling of NiTi architectured materials. Both structures are compressed quasi-statically by two horizontal rigid planes. The contact between rigid planes and the architectured material is assumed to be a surface-to-surface contact with a tangential frictional coefficient of 0.2. The bottom plane was completely fixed by the reference point and the top plane moved downward until the macroscopic strain reached the maximum value before returning to the initial position. The same C3D8R element with an approximate seed size smaller than 0.14 mm is used to discretize the geometry model after the mesh convergence study. A one-quarter model with *x-z* and *y-z* plane symmetry is used to reduce computational time. The macroscopic engineering stress and strain were calculated from the reaction force and displacement of the reference point of the top plane.

3. Materials and methods

3.1. Materials and additive manufacturing

The NiTi architectured materials and cylindrical bulk samples were

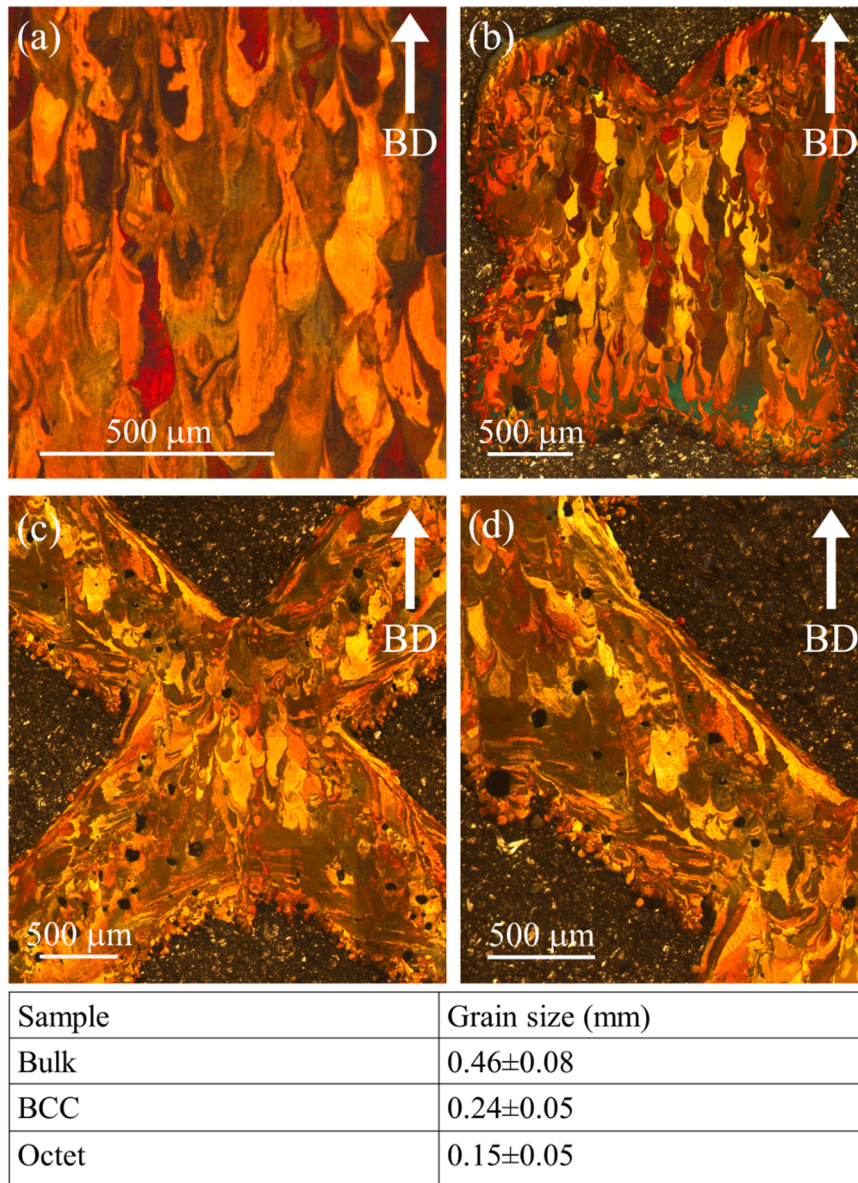| Sample	Grain size (mm)
Bulk	0.46±0.08
BCC	0.24±0.05
Octet	0.15±0.05

Fig. 7. Optical images of the microstructure for (a) Bulk (b) BCC structure (c) octet structure and (d) magnified strut in octet structure and corresponding grain size.

manufactured by a laser-based powder bed fusion (L-PBF) process using an Aconity3D Midi printer equipped with a fiber ytterbium laser (1060 nm wavelength). Cylindrical samples of 13 mm diameter and 20 mm length were fabricated for material properties calibration. The $20 \times 20 \times 20$ mm^3 architectured material samples with $5 \times 5 \times 5$ tessellation were manufactured for microstructural characterization and subsequent mechanical tests. Commercial Ni$_{51.4}$Ti$_{48.6}$ powder prepared by gas atomization was used as powder bed feedstock. The process chamber was filled with high-purity Argon. A stripe scanning strategy with a rotation of 67.5° between layers was used to heat and fuse the powder bed as shown in Fig. 3(a) and (b). The process parameters were optimized to mitigate macroscopic defects such as cracks, warping and delamination. based on our earlier research [29,48]. The process parameters, resulting in a defect-free sample were selected for this study and are listed in Table 2.

3.2. Microstructural characterization

The actual relative density of additively manufactured architectured materials was calculated by the ratio of their measured density to the theoretical density of base NiTi material (6.450 g/cm^3). Strut diameter was measured using a Keyence VHX-5000 optical microscope. Metallographic samples were cut using Electrical Discharge Machining (EDM) with exposed surfaces as shown in Fig. 3(a). EDS (Energy Dispersive Spectroscopy) samples use the macroscopic (110) surface of the BCC structure and (100) surface of the octet structure because compositional deviations along the struts were taken into account. The macroscopic (100) surfaces, which are parallel to the building direction of the L-PBF process, were further used for microstructural characterization. These samples were ground and polished following standard procedures used for the metallographic preparation of metal samples. Samples were subsequently etched using a solution consisting of 120 ml distilled water, 15 ml HCl, 15 g Na$_2$S$_2$O$_5$, 10 g K$_2$S$_2$O$_5$ and 2 g NH$_4$-HF to identify austenite grains. Austenite grains were visualized by linearly polarized light (LEICA DML 5000 light optical microscope). The grain size of columnar grains is estimated using the image software ImageJ. EDS analysis (using SEM, JEOL JSM 6500 F) was performed on seven different locations and calculated as the mean and deviation. Phase transformation temperatures were measured by a differential scanning calorimetry (DSC, Perkin Elmer DSC 800) in a nitrogen atmosphere with
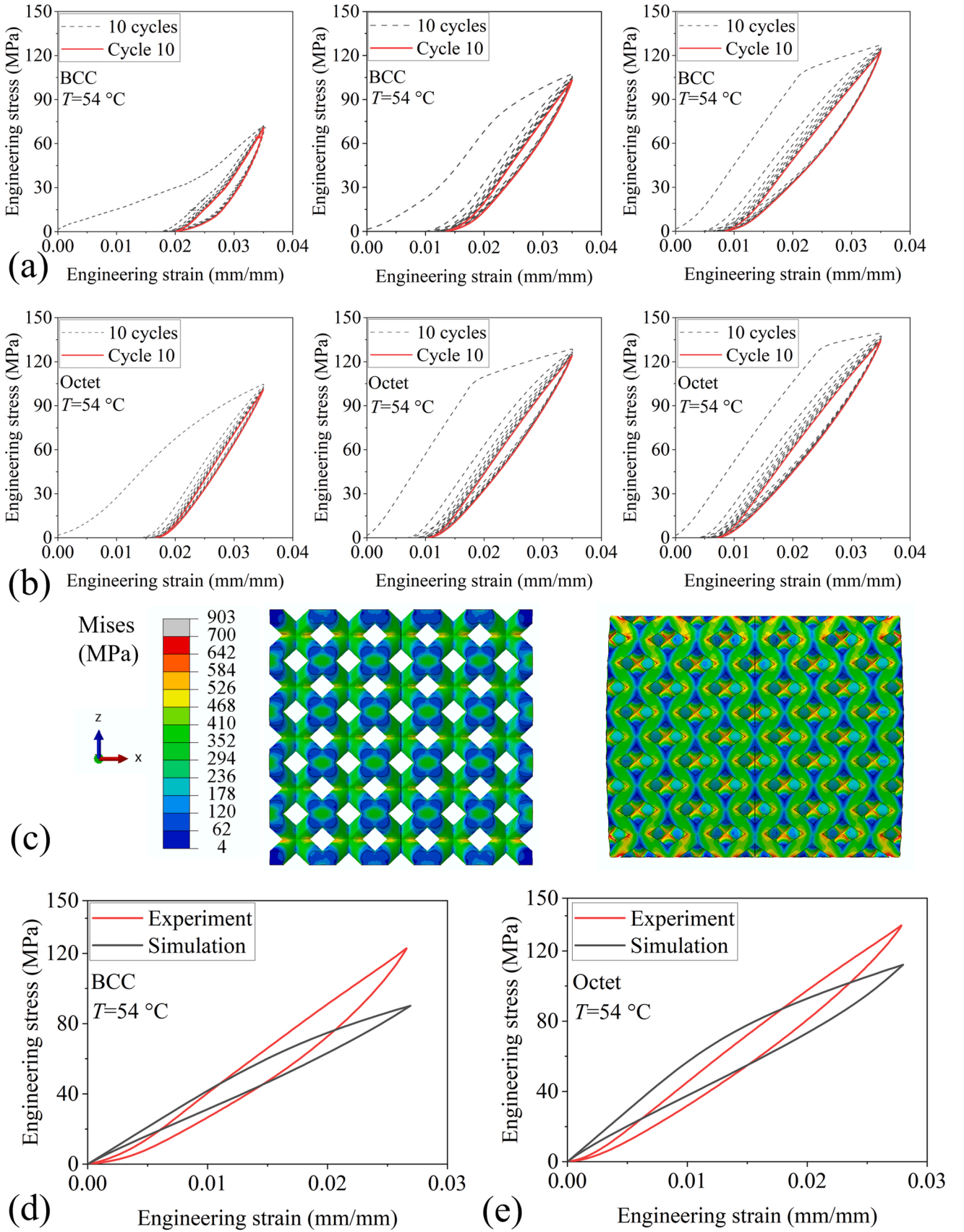
Fig. 8. Cyclic compression tests on (a) BCC and (b) octet structure, (c) von Mises stress distribution after symmetric operation in post-processing and (d) validation of simulation in the 10th cycle under cyclic compression tests.
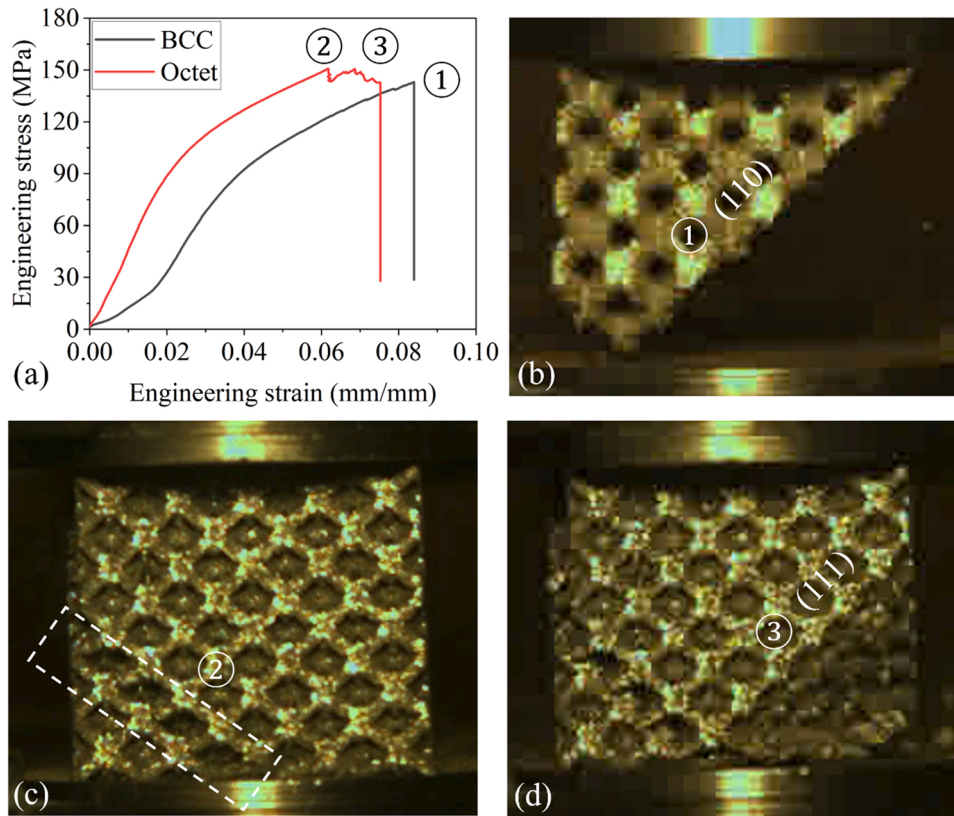
Fig. 9. (a) Uniaxial fracture compression tests and high speed camera images of (b) BCC structure and (c) (d) octet structure.

a cooling and heating rate of 10 °C/min over a temperature range of − 50 to + 150 °C. The austenite start temperature (A_s), austenite finish temperature (A_f), martensite start temperature (M_s) and martensite finish temperature (M_f) were determined using the tangential lines.

3.3. Mechanical testing

To characterize the printed NiTi bulk material, cuboid samples (Section 4.2 cross-section of 4.2 mm × 4.2 mm, height of 8 mm) were cut from the as-fabricated cylindrical samples with a diameter of 13 mm, using EDM. Compression tests were conducted at a strain rate of 1.0×10^{-4} s^{-1}, using a 25 kN MTS 858 hydraulic test machine, equipped with a high temperature extensometer (632.53 F-14, MTS). A sample temperature of 54 °C was maintained by locating the sample inside the coil of an induction heating system with the temperature being controlled by a K-type thermocouple (spot welded to the specimen). Displacement-controlled cyclic loading was applied to the sample with a maximum strain of 8 %.

The cyclic compressive response of NiTi architectured materials was investigated using universal mechanical tests (Zwick Z100). The samples were placed inside a heating chamber with a constant temperature of 54 °C. To determine the recoverable strain accurately, engineering strains of architectured materials were measured using a contact extensometer (Zwick DigiClip with a gauge length of 24 mm). Cyclic compression tests were conducted three times, with each test containing 10 cycles so that the superelasticity of architectured materials was stabilized. Displacement-controlled loading was applied with a maximum displacement of 0.7 mm and a strain rate of 5×10^{-4} s^{-1}. The fracture behavior of designed NiTi architectured materials was investigated using compressive deformation until fracture. The fracture images were taken using a high speed camera. The engineering strain was measured using a contact extensometer (MakroExtensometer BTC EXMACRO.001).

The local mechanical properties of different NiTi samples were tested using instrumented indentation (Zwick ZHU2.5) at room temperature. A spherical ball indenter with a diameter of 0.5 mm was used to reduce the strain gradient. Hold time at the maximum force was set at 2 s and the indentation rate was 0.05 N/s. Indentation forces of 5, 10, 20 and 40 N were used to test the superelastic behavior and recoverability under indentation.

4. Results

4.1. Effective superelastic response

The superelastic response of RVEs with different relative densities ranging from 0.1 to 0.6 are modeled. Examples of effective stress and strain graphs of both RVEs with the relative density of 0.4 for uniaxial compression, shear and hydrostatic loading conditions are shown in Fig. 4. The octet structure shows higher stiffness and larger stress hysteresis than the BCC structure under uniaxial compression. Under hydrostatic loading, each strut in the structures is subjected to axial compression and both structures show a similar response. The BCC structure exhibits higher shear stiffness than the octet structure.

Initial transformation behavior under different loading conditions requires additional attention. The initial transformation stress, including uniaxial martensite transformation stress σ_M, shear martensite transformation stress τ_M and hydrostatic martensite transformation stress σ_{HM} were obtained using effective stress and strain curves of RVEs. All initial transformation stress are determined based on the effective martensite volume fraction $\bar{\xi} \geq 10^{-4}$ to reduce the numerical sensitivity of the single element. The uniaxial martensitic transformation stress σ_M obtained using RVE simulation is shown in Fig. 5 and the shear martensite transformation stress τ_M and hydrostatic martensite transformation σ_{HM} are shown in Fig. A. 2 and Fig. A. 3. It was found that the effective transformation stress is linearly dependent on environmental
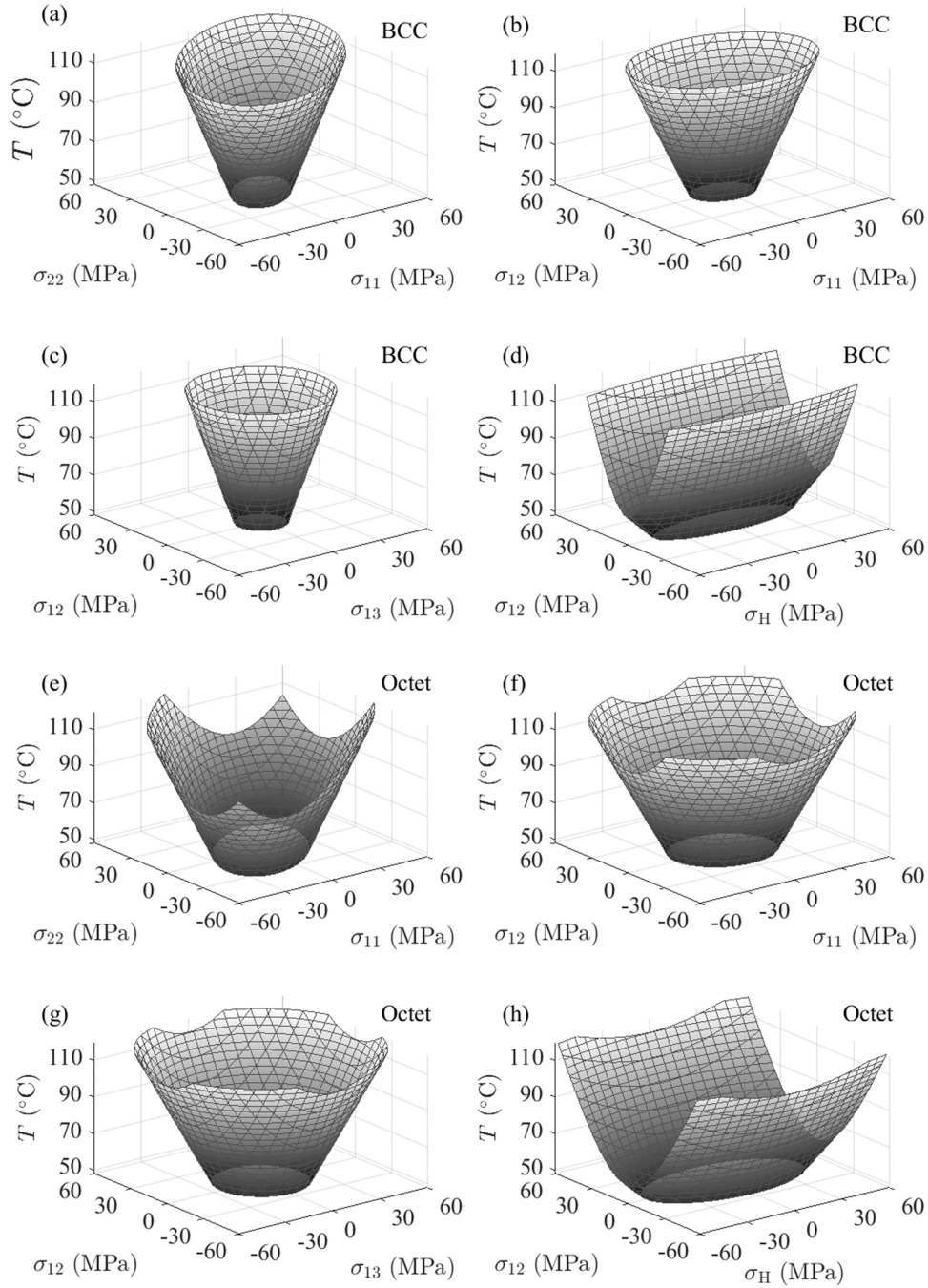
Fig. 10. Anisotropic initial transformation surface in (a)(e) (σ_{11}, σ_{22}), (b)(f) (σ_{11}, σ_{12}), (c)(g) (σ_{12}, σ_{13}), (d)(h) (σ_{12}, σ_H) and T loading space of BCC and octet structures.

temperature as shown in Fig. 5(a) and (c). Similar to the Clausius–Clapeyron relation for bulk NiTi in Eq. 3, the effective transformation–temperature relation is fitted for RVEs with different relative densities. The transformation stress is fitted to a power law, including the temperature effect:

$$\overline{\sigma_{Ms}} = k_1(\overline{\rho})^{p_1}\sigma_{Ms} - \overline{C_{AS}}T, \ \text{with} \ \overline{C_{AS}} = k_2(\overline{\rho})^{p_2}C_{AS} \quad (7)$$

Eq. (7) is an effective stress-relative density relation. The rescaled relation returns to the power dependence of uniaxial yield stress of traditional BCC and octet structures with high relative density [18] after the temperature effect is separated in the second term on the right-hand side. The BCC structure exhibits a combined deformation mode due to the non-slender beam used in architecture with high relative density

(Table 3). With increasing beam slenderness, this effective transformation stress-density power law can be varied. For both structures with low relative density, the analytical model of initial transformation stress based on slender beam theory is shown in Appendix A. These numerical results illustrate NiTi architectured material exhibiting effective transformation stress tailorable by adapting the relative density and cell architecture, which is rarely found in bulk NiTi alloys [2].

4.2. Microstructural characterization

In order to reduce the influence of microstructure in a single track, BCC and octet structures with a relative density of 0.4 were additively manufactured and tested (Fig. 3(c)). With this relative density, each
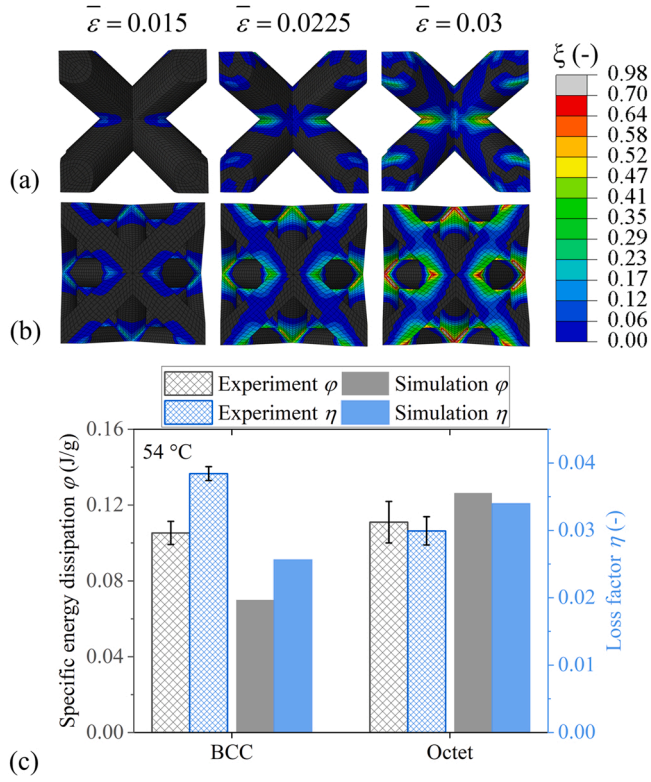
Fig. 11. Progressive martensitic transformation in (a) the BCC and (b) the octet structures, and (c) specific energy dissipation and loss factor of BCC and octet NiTi structures.

strut contained multiple scanning tracks and layers. The dimensional accuracy of both L-PBFed architectured materials is shown in Table 4. The dimensional discrepancy between the nominal and measured geometry of as-fabricated materials is due to partially molten powders, resulting in the waviness and roughness of struts [49]. The 'staircase effect' is another common AM phenomenon that influences the geometrical inaccuracy of as-fabricated architectured materials [38].

The martensitic transformation of NiTi is known to be sensitive to Ni evaporation at high heat input in the L-PBF process [2]. EDS analyses were conducted on the (110) cross-section of BCC structures and (100) cross-section of octet structures and similar compositional ratios were detected, as shown in Table 5. Similar elemental composition results in less variation of superelastic behavior of constituent NiTi material in different structures. Martensitic transformation temperatures are obtained by DSC curves and shown in Table 6. As can be seen in Fig. 6, L-PBF architectured materials show a broader transformation temperature range and higher transformation temperatures compared to bulk samples. Higher reversed transformation temperatures are found in the octet structure than in the BCC structure. The influence of varying TTs

on the macroscopic functional properties of printed architectured materials is discussed in session 5.2.

The microstructure on the (100) cross-section parallel to the building direction (BD) of bulk, BCC and octet samples is shown in Fig. 7. NiTi samples printed with high Ni-rich raw powder ($Ni_{51.4}Ti_{48.6}$, at. %) show more macroscopic defects such as cracking, warping and delamination due to the change of element ratios [31]. In this work, high energy input (88.9 J/mm^3) was successfully used to mitigate these macroscopic defects based on bulk process optimization, as shown in Fig. 7(a). Pores defects are observed in as-fabricated architectured materials although bulk samples with low porosity were fabricated using the same process parameters. Coarse columnar grains epitaxially grow along the building direction (BD) in the bulk sample due to heat sinking into the as-fabricated layers [50]. Columnar grains growing along BD have an average length of 0.46 ± 0.08 mm, which surpasses multiple deposition layers (0.030 mm per layer). Similar epitaxial growth of coarse columnar grains is shown at the nodes of BCC and octet structures, which implies similar thermal dissipation conditions in bulk samples and nodes of architectured materials (Fig. 7(b) and (c)). The average length of columnar grain is 0.24 ± 0.05 mm in the BCC node and 0.15 ± 0.05 mm in the octet node. Fig. 7(d) illustrates the microstructure of a strut of octet structure, which is on the macroscopic (100) cross-section and 45° to the BD. Three different areas of grains with different growth orientations are distinguishable. At both edges of the strut, thin columnar grains grow along the orientation of the strut. The growth direction of columnar grains gradually transforms to BD around the middle axis. The influence of microstructure on local elastic properties is compared using instrumented indentation as shown in Fig. C. 2.

4.3. Uniaxial compression tests

The superelastic response of both structures was tested using three batches of cyclic compression tests under the displacement loading of 0.7 mm, as shown in Fig. 8(a) and (b). In each training batch, the superelastic response of NiTi architectured materials was achieved with a large recoverable strain. The recoverable strain and stress hysteresis increased in the second and third training, while hardening behavior is observed in the first cycle. To distinguish the hardening behavior and stress plateau in both structures, the von Mises stress distribution of $5 \times 5 \times 5$ cells simulation after symmetric operation in post-processing is shown in Fig. 8(c). The relative density of ideal structures is approximated as 0.5 considering the geometrical inaccuracy of as-fabricated architectured material as shown in Table 4. The printed NiTi does not reach plastic yield until 1151 MPa as shown in Fig. 1(d), and as can be seen in the stress contour, no stress-concentration-induced plastic stress is shown. The stress plateau and hardening in the training process are mainly attributed to the stress-induced martensitic transformation and transformation-induced plasticity. After 10 training cycles, the stress plateau disappears and a stabilized superelastic response is achieved. Due to the inhomogeneous stress distribution in NiTi architectured materials, insufficient martensitic transformation in the first cyclic test
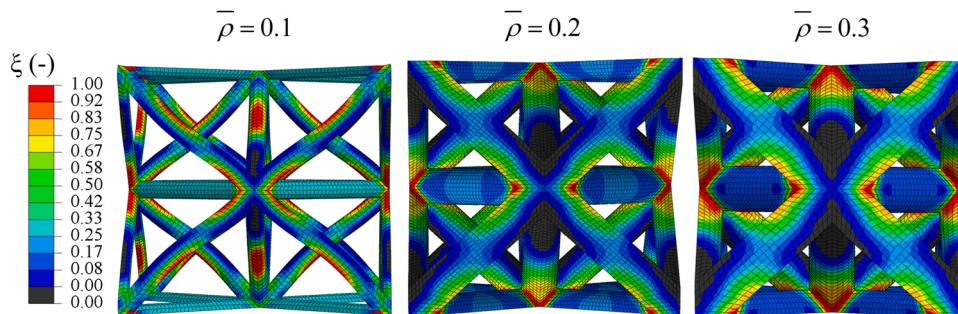

Fig. A1. Transition of deformation mode due to the formation of superelastic hinges.
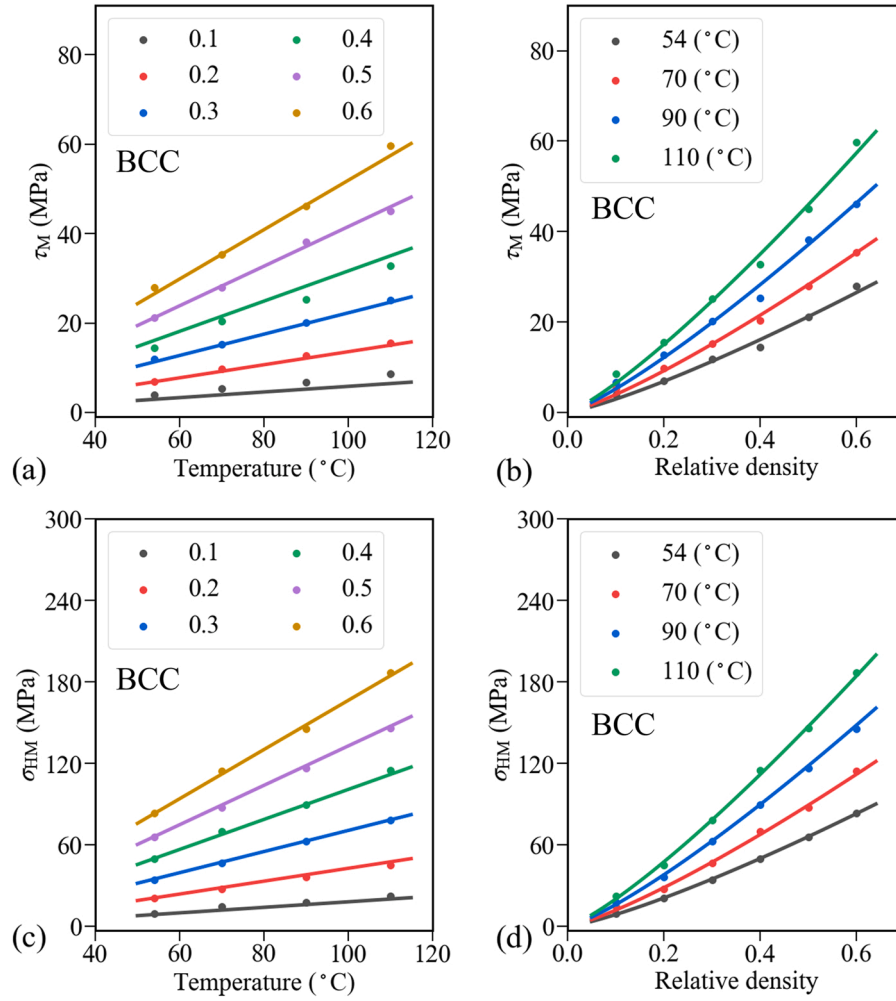
Fig. A2. Effect of relative densities and temperature loadings on martensite start stress of BCC structure under (a) shear and (b) hydrostatic loadings.

results in low recoverable strain. It is likely due to the incompatibility of preferred martensite variants and the nonuniform stress distribution in NiTi structures. The experimental and numerical results are compared in Fig. 8(d) and (e). Due to the hardening behavior in the training process, the tested samples show higher stiffness than the numerical results. Strain hardening is more obvious in the cyclic compression of the BCC structure than in the octet structure as shown in Fig. 7(a) and (b), which implies that the martensite re-orientation process is more favorable in stretching-dominated octet structures with a larger portion of axial loading [50].

Under high displacement loading, the strength of NiTi is reached. Different from reported architectured materials with lower relative density, designed herein structures lose stability and self-supported configuration once the strength of the structures is reached. The sudden fracture and drop in engineering stress were recorded as shown in Fig. 9(a) and supplementary videos. The fracture deformation is illustrated along the macroscopic (100) shear plane for the BCC structure (Fig. 9(b)) and the (111) shear plane for the octet structure (Fig. 9(c) and (d)). The superelastic behavior in NiTi architectured material is generally constrained by the strength of the base NiTi material, so the complete martensitic transformation is prevented. Although further martensitic transformation can be induced by larger displacement loading, plastic deformation and damage at the stress concentration areas may result in the fracture of the entire structure.

5. Discussion

5.1. Initial transformation surface

For architectured materials with orthotropic symmetry, the anisotropic initial transformation behavior is described using the extended Hill's model [15]:

$$A(\sigma_{11} - \sigma_{22})^2 + B(\sigma_{22} - \sigma_{33})^2 + C(\sigma_{22} - \sigma_{33})^2 + D\sigma_{12}^2 + E\sigma_{23}^2 + F\sigma_{13}^2 + G\sigma_H^2 = 1,$$

(8)

where A-G are anisotropy coefficients that are obtained by curve fitting under uniaxial, shear and hydrostatic loading conditions. Because the environmental temperature is considered as the temperature loading and included in Eqs. (9–10), multiaxial stress is not directly normalized using uniaxial transformation stress. G is obtained under hydrostatic loading, $A = B = C$ are obtained under uniaxial loading and $D = E = F$ are obtained under shearing loading conditions [51], which are given in Appendix B. For the choice of $\overline{\rho} = 0.4$, A-G are given explicitly: For BCC structure,

$$G = (50.12 + 1.10(T - T_0))^{-2}$$
$$A = (20.49 + 0.46(T - T_0))^{-2}$$
$$D = (16.09 + 0.34(T - T_0))^{-2}$$
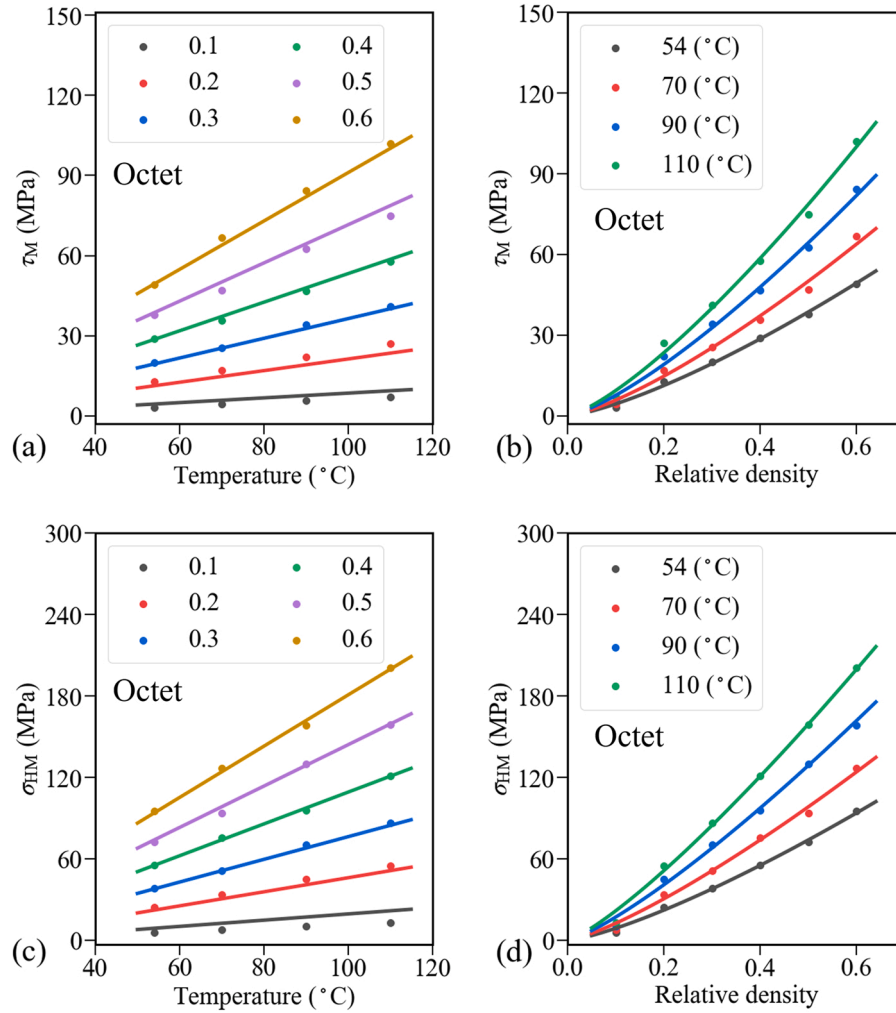
(9)

For the octet structure,

Fig. A3. Effect of relative densities and temperature loadings on martensite start stress of octet structure under (a) shear and (b) hydrostatic loadings.

$$G = (55.43 + 1.17(T - T_0))^{-2}$$
$$A = (30.97 + 0.51(T - T_0))^{-2},$$
$$D = (28.63 + 0.54(T - T_0))^{-2}$$

(10)

where T_0 is the reference temperature. For the BCC and octet structures with $\bar{\rho} = 0.4$, an anisotropic initial transformation surface is shown in Fig. 10. Projecting (σ_{11}, σ_{12}, T) transformation surface onto (σ_{11}, T) plane, the anisotropic transformation surface reduces to the linear dependent relation between uniaxial stress and temperature. The anisotropy of NiTi lattice-based architectured materials does not depend on temperature. The transformation stress and linear dependence relation can be tailored by relative density and cell architectures. The proposed rescaled density-properties graph and effective transformation behaviors provide a physical understanding of the design parameters of NiTi architectured materials.

5.2. Recoverable energy absorption and deformation mechanism

The superelastic response of NiTi architectured materials is modeled and experimentally obtained as shown in Section 4.3. This superelastic stress hysteresis can be used for cyclic energy absorption. Energy dissipation is defined as the closed integration of the effective stress and strain curve and the specific energy dissipation is formulated as

$$\varphi = \frac{\Delta W}{\rho} = \frac{\oint \overline{\sigma} d\overline{\varepsilon}}{\rho},$$

(11)

where ρ is the density of architectured materials and ΔW is the energy dissipation. Cyclic energy dissipation can be formulated as damping due to the nature of dissipative energy. For metallic damping cases, the loss factor η is defined from the uniaxial compression test as

$$\eta = \frac{\psi}{2\pi}, \ with \ \psi = \frac{\Delta W}{W} = \frac{\oint \overline{\sigma} d\overline{\varepsilon}}{\int_0^{\overline{\varepsilon}_{max}} \overline{\sigma} d\overline{\varepsilon}},$$

(12)

where ψ is the specific damping capacities and W is the storage energy [52].

Conventional metallic architectured materials exhibit energy absorption due to permanent plastic deformation [17,53]. NiTi architectured materials can provide stable nonlinear stiffness and recoverable energy dissipation under cyclic compressive loading as shown in Fig. 8 (d), (e) and Fig. 11. Damping in cellular material is amplitude-dependent, but mainly results from the irreversible process of microplastic deformation. Due to the strain concentration in truss-based architectured materials, microplastic strain occurs at the strut junctions before the effective stress reaches macroscopic yield stress [13,14]. This microplastic strain results in irreversible damage instead of a reversible stress hysteresis. In NiTi architectured materials, detwinning deformation is used to replace dislocation deformation to obtain damping. For architectured materials with high relative density, structures are interconnected by non-slender beams and stable structure configuration under uniaxial compression is supported by strut intersection (without rotation and buckling of struts). Different from the nearly homogeneous
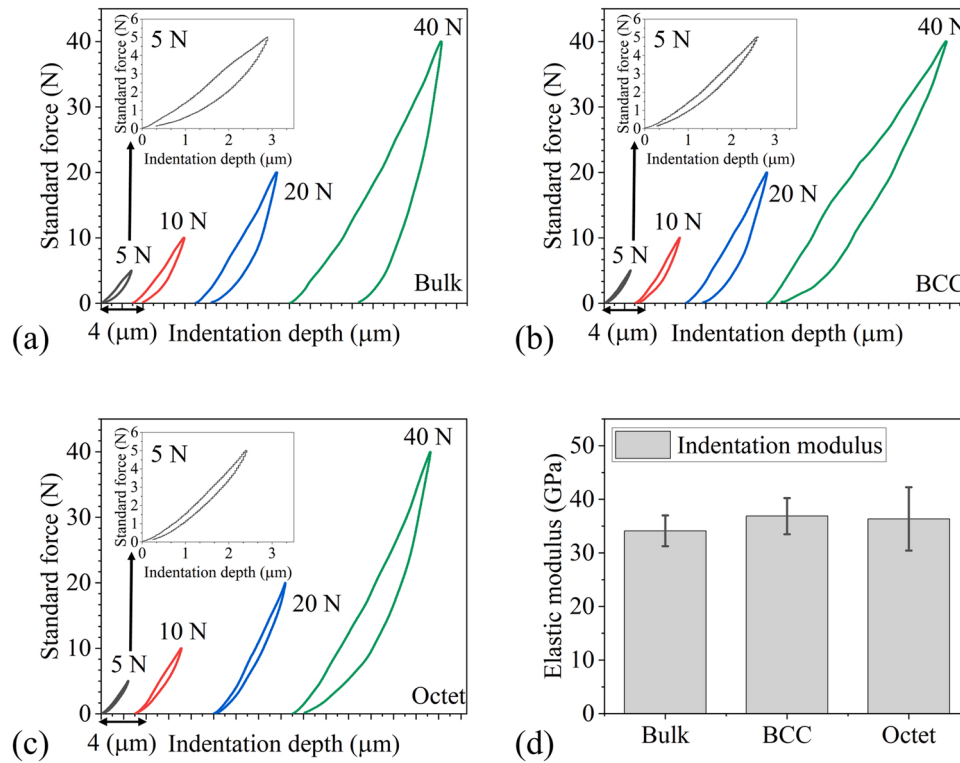
Fig. C2. Instrumented indentation force and depth curves of (a) bulk, (b) BCC and (c) octet samples and (d) indentation modulus.
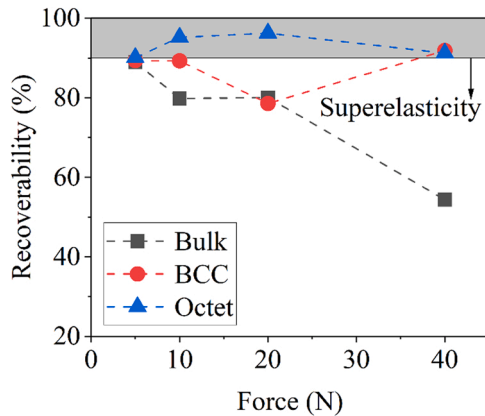

Fig. C1. Recoverability of instrumented indentation.

transformation in NiTi bulk sample, martensitic transformation in NiTi architectured materials is inhomogenous and induced by stress concentration at the nodes. Similar to the plastic deformation behavior of both structures, superelastic hinges first form at the nodes and are further connected by a progressive martensitic transformation zone along the struts. Progressive martensitic transformation contributes to the recoverable strain and energy dissipation.

Due to the large recoverable strain and energy dissipation in NiTi constitutive relation, the advantages of classic deformation modes need to be further discussed. One clear conclusion from theoretical results is that stretching-dominated deformation enables sufficient martensitic transformation and broader stress hysteresis. Bending-dominated deformation enhances compliance of base NiTi but the superelastic deformation is constrained by the stress concentration and yield stress of base NiTi. Comparative numerical results between BCC and octet structures validate this basic conclusion for NiTi structure by illustrating larger energy dissipation in stretching-dominated octet structure. Future

design research can choose the main deformation mode compatible with the hysteresis or compliant application of NiTi structure.

The experiments illustrate that BCC structures exhibit comparable energy dissipation and higher loss factor than octet structures, which is different from the prediction based on the numerical model. The indentation modulus of bulk, BCC and octet samples are comparable as shown in Appendix C, which proves the effectiveness of the using bulk sample in calibration.

The phenomenological model cannot capture the local variations in the TTs due to the inhomogeneous nature of the L-PBF process. Although the same process strategy and raw powder are used, different thermal history induced by path-by-path laser scanning in different structures results in the variation of Ni evaporation and microstructure in the deposition layer, as shown in Table 5 and Fig. 7. Comparable Ni contents were found in both structures, while BCC structure has a larger grain size than octet structure. It is reported that TTs generally decrease with the increase in grain size [54]. Lower TTs in the BCC structure result in a larger portion of stress-induced martensite when the same $T = 54\ °C$ was used in compression tests, so a larger stress hysteresis area can be obtained in the BCC structure. From the view of the deformation mode, the octet structures exhibit higher energy dissipation capacity and damping capacity, but a higher loss factor was illustrated in the BCC structure. The influence of NiTi local microstructure surpasses the deformation modes, and thus further research should be conducted to control microstructure-sensitive thermomechanical properties of NiTi architectured materials. Our combined numerical and experimental work illustrates the importance of accounting for the effect of local microstructure variations on the thermomechanical properties functionalities of NiTi architectured material, which is still to be further investigated.

6. Conclusions

In the present study, Ni-rich NiTi BCC and octet structures with superelasticity and damping behavior are successfully designed,

modeled and fabricated using L-PBF. Anisotropic and temperature-dependent superelasticity of NiTi BCC and octet structures are investigated using validated FEM and uniaxial compression testing. The following conclusions can be drawn:

- Effective transformation stress of NiTi BCC and octet structures was found to be dependent on relative density and temperature. Effective Clausius–Clapeyron relationships are tailorable by relative density and internal architecture of the unit cell. The martensitic transformation surface for NiTi BCC and octet structures was approximated using extended Hills criteria considering the temperature effect. The anisotropy of NiTi lattice-based architectured materials is not influenced by temperature.
- NiTi BCC and octet structures, designed herein, were successfully fabricated by L-PBF and mechanically tested. High energy input (88.9 J/mm^3) was used to mitigate macroscale cracking and warping. EDS results show a comparable Ni/Ti ratio between bulk, BCC and octet samples. Coarse columnar grains were found to grow epitaxially in the bulk and at the nodes of architectured material.
- NiTi BCC and octet structures exhibit stabilized superelasticity with recoverable strain up to 2.8 %. The BCC structure shows fracture along (110), while the octet structure shows fracture along (111) surface under large deformation.
- Stretching-dominated deformation enables sufficient martensitic transformation and broader stress hysteresis. Bending-dominated deformation enhances compliance of base NiTi but the superelastic deformation is constrained by the stress concentration and yield stress of base NiTi.
- NiTi BCC and octet structures exhibit reversible energy dissipation and damping due to progressive martensitic transformation. Under uniaxial compression loading, superelastic hinges form at the nodes and martensitic transformation gradually extends from the node along the struts. Different from theoretical prediction, BCC structure shows higher comparable energy dissipation and higher loss factor due to lower transformation temperatures. Increasing the grain size in the BCC structure leads the lower TTs. Further research will be conducted to control the superelastic response by tailoring the microstructure.

Designed and validated herein NiTi architectured materials exhibit recoverable energy absorption without external thermal stimulus, which can be used in shock and vibration protection under cyclic loading. This adaptivity and functionality of NiTi architectured material make it suitable for industrial applications in aerospace, maritime and automotive industries.

CRediT authorship contribution statement

Jovanova Jovana: Writing – review & editing, Supervision. **Popovich Vera:** Writing – review & editing, Supervision. **Zhu Jia-Ning:** Writing – review & editing, Investigation, Formal analysis. **Yan Zhaorui:** Writing – original draft, Methodology, Investigation, Formal analysis, Conceptualization. **Riemslag Ton:** Methodology, Investigation. **Borisov Evgenii:** Investigation. **Hermans Marcel:** Writing – review & editing, Supervision. **Scott Sean Paul:** Methodology, Investigation.

Declaration of Competing Interest

The authors declare that they have no known competing financial interests or personal relationships that could have appeared to influence the work reported in this paper.

Data availability

Data will be made available on request.

Appendix A. Effective transformation behaviors

To understand the temperature effect on the effective transformation stress of both structures, the effective transformation stress is expressed as a function of relative density. Macroscopic plastic strain is substituted by the initial martensitic transformation of NiTi. Using the first-order approximation equation of relative density, the initial transformation stress of the BCC and octet structures under uniaxial compressive response can be obtained using slender beam theory:

$$\overline{\sigma_{\mathrm{Ms}}} = k(\overline{\rho})^p \sigma_{\mathrm{Ms}}^T, \tag{A.1}$$

where k and p are the architecture (strut orientation) dependent coefficients. $k = 0.47$ and $p = 1.5$ for BCC structure, and $k = 1/3$ and $p = 1$ for octet structure under uniaxial compression based on analytical models [16,55]. The 1-dimensional reduction of forward transformation stress is

$$\sigma_{\mathrm{Ms}}^T = \sigma_{\mathrm{Ms}} - C_{\mathrm{AS}}T. \tag{A.2}$$

The temperature-influenced term can be decomposed from effective transformation stress and expressed as

$$\overline{\sigma_{\mathrm{Ms}}} = k(\overline{\rho})^p \sigma_{Ms} - \overline{C_{\mathrm{AS}}}T, \text{ with } \overline{C_{\mathrm{AS}}} = k(\overline{\rho})^p C_{\mathrm{AS}}, \tag{A.3}$$

where $\overline{C_{\mathrm{AS}}}$ is the effective Clausius–Clapeyron relation. This material property can be controlled by relative density under uniaxial compression. To account for the influence of non-slender beams, the power law relation is modeled numerically using RVEs.

At the relative density of 0.1, the transition of the mesoscopic deformation mode is observed in the octet structure. An additional superelastic hinge is generated at the middle of the beam as shown in Fig. A1. Due to the superelastic buckling of the slender NiTi strut, the octet structure at the relative density of 0.1 loses stability. However, the elastic deformation of martensite can mitigate the twist of the lattice and reinforce the stability of the octet

structure [17]. The effective transformation stress under shear and hydrostatic loadings are shown in Fig. A2 and Fig. A3.

Appendix B. Anisotropic coefficients A-G in extended Hill's model

The anisotropic coefficient of extended Hill's model is given without normalization of uniaxial stress. For BCC structure,

$$
\begin{aligned}
G &= \left(0.563(\overline{\rho})^{1.25}\sigma_{\mathrm{Ms}} + 0.519(\overline{\rho})^{1.22}C_{\mathrm{AS}}(T - T_0)\right)^{-2} \\
A &= \frac{4}{9}\left(0.424(\overline{\rho})^{1.92}\sigma_{\mathrm{Ms}} + 0.426(\overline{\rho})^{1.96}C_{\mathrm{AS}}(T - T_0)\right)^{-2}. \\
D &= \left(0.178(\overline{\rho})^{1.23}\sigma_{\mathrm{Ms}} + 0.157(\overline{\rho})^{1.21}C_{\mathrm{AS}}(T - T_0)\right)^{-2}
\end{aligned}
\tag{B.1}
$$

For octet structure,

$$
\begin{aligned}
G &= \left(0.654(\overline{\rho})^{1.30}\sigma_{\mathrm{Ms}} + 0.530(\overline{\rho})^{1.17}C_{\mathrm{AS}}(T - T_0)\right)^{-2} \\
A &= \frac{4}{9}\left(0.368(\overline{\rho})^{1.31}\sigma_{\mathrm{Ms}} + 0.254(\overline{\rho})^{1.27}C_{\mathrm{AS}}(T - T_0)\right)^{-2}, \\
D &= \left(0.351(\overline{\rho})^{1.34}\sigma_{\mathrm{Ms}} + 0.270(\overline{\rho})^{1.29}C_{\mathrm{AS}}(T - T_0)\right)^{-2}
\end{aligned}
\tag{B.2}
$$

where reference temperature T_0 is set to be 54 °C.

Appendix C. Instrumented indentation

Inhomogeneous microstructure results in the variation of mechanical properties of the base NiTi material. This variation of mechanical properties leads to discrepancies between numerical simulation and validation experiments. To reveal the local mechanical properties of the base NiTi material, instrumented indentation was conducted under room temperature and low loading conditions. Indentation force and depth curves of different structures with varying maximum forces of 5 N, 10 N, 20 N and 40 N are shown in Fig. C2. For the bulk sample, residual depth increased with indentation force because the superelastic deformation could not recover at a room temperature lower than A_{f}. Higher recovery capacities are found in the center of BCC and octet cross-section samples due to the inhomogeneous microstructure and martensitic transformation temperatures. The indentation force of 5 N is chosen to estimate the indentation elastic modulus due to the high proportion of elastic deformation. The estimation of the indentation elastic modulus is based on Kumar's simplification of the classical Hertz model [56]. Within the restriction condition of the Hertz model [57], the indentation force and depth relation for the ball indenter is

$$
P = \frac{4}{3}R_{\mathrm{eff}}^{1/2}E_{\mathrm{ind}}h_{\mathrm{R}}^{3/2},
\tag{C.1}
$$

where R_{eff} is the effective radius of curvature at the contact. R_{eff} can be given as

$$
\frac{1}{R_{\mathrm{eff}}} = \frac{1}{R} - \frac{1}{R_{\mathrm{S}}},
\tag{C.2}
$$

where R is the radius of the ball indenter and R_{S} is the residual radius of indentation. To apply this method to superelastic NiTi, high-depth recoverability is required and elastic deformation is dominant as shown in Fig. C1 [58]. R_{eff} is approximated to R and h_{R} is approximated to the maximum indentation depth h_{max}. Equation (C.1) is approximated to

$$
P = \frac{4}{3}R^{1/2}E_{\mathrm{ind}}h_{\mathrm{max}}^{3/2}.
\tag{C.3}
$$

This method provides an approximated comparison of local mechanical properties at the mesoscale between different NiTi samples. material thermomechanical properties used in FEM should be carefully calibrated using uniaxial loading tests.

The indentation force and depth curves of bulk, BCC and octet samples are shown in Fig. C. 2. Indentation with a force of 5 N is repeated in four different locations and the estimated elastic modulus of the bulk and structural samples are shown in Fig. C. 2 (d). The indentation elastic modulus of BCC and octet structures are comparable with the indentation elastic modulus of the bulk sample. The variation of indentation modulus is likely influenced by local microstructure in different locations.

Appendix D. Supporting information

Supplementary data associated with this article can be found in the online version at doi:10.1016/j.addma.2023.103505.

References

[1] J. Mohd Jani, M. Leary, A. Subic, M.A. Gibson, A review of shape memory alloy research, applications and opportunities, Mater. Des. 56 (2014) 1078–1113, https://doi.org/10.1016/j.matdes.2013.11.084.

[2] M. Elahinia, N. Shayesteh Moghaddam, M. Taheri Andani, A. Amerinatanzi, B. A. Bimber, R.F. Hamilton, Fabrication of NiTi through additive manufacturing: a review, Prog. Mater. Sci. 83 (2016) 630–663, https://doi.org/10.1016/j.pmatsci.2016.08.001.

[3] N.B. Morgan, Medical shape memory alloy applications – the market and its products, Mater. Sci. Eng. A 378 (2004) 16–23, https://doi.org/10.1016/j.msea.2003.10.326.

[4] D.C. Lagoudas, Shape Memory Alloys: Modeling and Engineering Applications, Springer, 2008.

[5] Z. jue Tang, W. wei Liu, Y. wen Wang, K.M. Saleheen, Z. chao Liu, S. tong Peng, Z. Zhang, H. chao Zhang, A review on in situ monitoring technology for directed energy deposition of metals, Int. J. Adv. Manuf. Technol. 108 (2020) 3437–3463, https://doi.org/10.1007/s00170-020-05569-3.

[6] X. Zhang, A. Vyatskikh, H. Gao, J.R. Greer, X. Li, Lightweight, flaw-tolerant, and ultrastrong nanoarchitected carbon, Proc. Natl. Acad. Sci. USA 116 (2019) 6665–6672, https://doi.org/10.1073/pnas.1817309116.

[7] J. Feng, B. Liu, Z. Lin, J. Fu, Isotropic octet-truss lattice structure design and anisotropy control strategies for implant application, Mater. Des. 203 (2021), 109595, https://doi.org/10.1016/j.matdes.2021.109595.

[8] T. Tancogne-Dejean, M. Diamantopoulou, M.B. Gorji, C. Bonatti, D. Mohr, 3D plate-lattices: an emerging class of low-density metamaterial exhibiting optimal isotropic stiffness, Adv. Mater. 30 (2018) 1–6, https://doi.org/10.1002/adma.201803334.

[9] K. Karami, A. Blok, L. Weber, S.M. Ahmadi, R. Petrov, K. Nikolic, E.V. Borisov, S. Leeflang, C. Ayas, A.A. Zadpoor, M. Mehdipour, E. Reinton, V.A. Popovich, Continuous and pulsed selective laser melting of Ti6Al4V lattice structures: effect of post-processing on microstructural anisotropy and fatigue behaviour, Addit. Manuf. 36 (2020), 101433, https://doi.org/10.1016/j.addma.2020.101433.

[10] L. Zhang, S. Feih, S. Daynes, S. Chang, M.Y. Wang, J. Wei, W.F. Lu, Energy absorption characteristics of metallic triply periodic minimal surface sheet structures under compressive loading, Addit. Manuf. 23 (2018) 505–515, https://doi.org/10.1016/j.addma.2018.08.007.

[11] T. Tancogne-Dejean, D. Mohr, Stiffness and specific energy absorption of additively-manufactured metallic BCC metamaterials composed of tapered beams, Int. J. Mech. Sci. 141 (2018) 101–116, https://doi.org/10.1016/j.ijmecsci.2018.03.027.

[12] A. du Plessis, S.M.J. Razavi, M. Benedetti, S. Murchio, M. Leary, M. Watson, D. Bhate, F. Berto, Properties and applications of additively manufactured metallic cellular materials: a review, Prog. Mater. Sci. 125 (2022), 100918, https://doi.org/10.1016/j.pmatsci.2021.100918.

[13] I.S. Golovin, H.R. Sinning, I.K. Arhipov, S.A. Golovin, M. Bram, Damping in some cellular metalic materials due to microplasticity, Mater. Sci. Eng. A 370 (2004) 531–536, https://doi.org/10.1016/j.msea.2003.08.089.

[14] I.S. Golovin, H.R. Sinning, J. Göken, W. Riehemann, Fatigue-related damping in some cellular metallic materials, Mater. Sci. Eng. A 370 (2004) 537–541, https://doi.org/10.1016/j.msea.2003.08.090.

[15] V.S. Deshpande, N.A. Fleck, M.F. Ashby, Effective properties of the octet-truss lattice material, J. Mech. Phys. Solids 49 (2001) 1747–1769, https://doi.org/10.1016/S0022-5096(01)00010-2.

[16] L. Dong, V. Deshpande, H. Wadley, Mechanical response of Ti-6Al-4V octet-truss lattice structures, Int. J. Solids Struct. 60 (2015) 107–124, https://doi.org/10.1016/j.ijsolstr.2015.02.020.

[17] T. Tancogne-Dejean, A.B. Spierings, D. Mohr, Additively-manufactured metallic micro-lattice materials for high specific energy absorption under static and dynamic loading, Acta Mater. 116 (2016) 14–28, https://doi.org/10.1016/j.actamat.2016.05.054.

[18] N. Jin, F. Wang, Y. Wang, B. Zhang, H. Cheng, H. Zhang, Failure and energy absorption characteristics of four lattice structures under dynamic loading, Mater. Des. 169 (2019), 107655, https://doi.org/10.1016/j.matdes.2019.107655.

[19] M. Dallago, S. Raghavendra, V. Luchin, G. Zappini, D. Pasini, M. Benedetti, The role of node fillet, unit-cell size and strut orientation on the fatigue strength of Ti-6Al-4V lattice materials additively manufactured via laser powder bed fusion, Int. J. Fatigue 142 (2021), 105946, https://doi.org/10.1016/j.ijfatigue.2020.105946.

[20] D. Qi, H. Yu, M. Liu, H. Huang, S. Xu, Y. Xia, G. Qian, W. Wu, Mechanical behaviors of SLM additive manufactured octet-truss and truncated-octahedron lattice structures with uniform and taper beams, Int. J. Mech. Sci. 163 (2019), 105091, https://doi.org/10.1016/j.ijmecsci.2019.105091.

[21] L. Liu, P. Kamm, F. García-Moreno, J. Banhart, D. Pasini, Elastic and failure response of imperfect three-dimensional metallic lattices: the role of geometric defects induced by selective laser melting, J. Mech. Phys. Solids 107 (2017) 160–184, https://doi.org/10.1016/j.jmps.2017.07.003.

[22] X. Li, C.C. Roth, T. Tancogne-Dejean, D. Mohr, Rate- and temperature-dependent plasticity of additively manufactured stainless steel 316L: characterization, modeling and application to crushing of shell-lattices, Int. J. Impact Eng. 145 (2020), 103671, https://doi.org/10.1016/j.ijimpeng.2020.103671.

[23] Z. Xiong, M. Li, S. Hao, Y. Liu, L. Cui, H. Yang, C. Cui, D. Jiang, Y. Yang, H. Lei, Y. Zhang, Y. Ren, X. Zhang, J. Li, 3D-printing damage-tolerant architected metallic materials with shape recoverability via special deformation design of constituent material, ACS Appl. Mater. Interfaces 13 (2021) 39915–39924, https://doi.org/10.1021/acsami.1c11226.

[24] W. Chen, D. Gu, J. Yang, Q. Yang, J. Chen, X. Shen, Compressive mechanical properties and shape memory effect of NiTi gradient lattice structures fabricated by laser powder bed fusion, Int. J. Extrem. Manuf. 4 (2022) 045002, https://doi.org/10.1088/2631-7990/ac8ef3.

[25] M.R. Karamooz Ravari, S. Nasr Esfahani, M. Taheri Andani, M. Kadkhodaei, A. Ghaei, H. Karaca, M. Elahinia, On the effects of geometry, defects, and material asymmetry on the mechanical response of shape memory alloy cellular lattice structures, Smart Mater. Struct. 25 (2016), https://doi.org/10.1088/0964-1726/25/2/025008.

[26] N. Van Viet, R. Abu Al-Rub, W. Zaki, Mechanical behavior of shape-memory alloy triply periodic minimal surface foam based on Schwarz primitive, J. Eng. Mech. 148 (2022) 1–12, https://doi.org/10.1061/(asce)em.1943-7889.0002130.

[27] W. Zaki, Z. Moumni, A three-dimensional model of the thermomechanical behavior of shape memory alloys, J. Mech. Phys. Solids 55 (2007) 2455–2490, https://doi.org/10.1016/j.jmps.2007.03.012.

[28] S. Saedi, N. Shayesteh Moghaddam, A. Amerinatanzi, M. Elahinia, H.E. Karaca, On the effects of selective laser melting process parameters on microstructure and thermomechanical response of Ni-rich NiTi, Acta Mater. 144 (2018) 552–560, https://doi.org/10.1016/j.actamat.2017.10.072.

[29] J.N. Zhu, E. Borisov, X. Liang, E. Farber, M.J.M. Hermans, V.A. Popovich, Predictive analytical modelling and experimental validation of processing maps in additive manufacturing of nitinol alloys, Addit. Manuf. 38 (2021) 101802, https://doi.org/10.1016/j.addma.2020.101802.

[30] L. Xue, K.C. Atli, S. Picak, C. Zhang, B. Zhang, A. Elwany, R. Arroyave, I. Karaman, Controlling martensitic transformation characteristics in defect-free NiTi shape memory alloys fabricated using laser powder bed fusion and a process optimization framework, Acta Mater. 215 (2021), 117017, https://doi.org/10.1016/j.actamat.2021.117017.

[31] L. Xue, K.C. Atli, C. Zhang, N. Hite, A. Srivastava, A.C. Leff, A.A. Wilson, D. J. Sharar, A. Elwany, R. Arroyave, I. Karaman, Laser powder bed fusion of defect-free NiTi shape memory alloy parts with superior tensile superelasticity, Acta Mater. 229 (2022), 117781, https://doi.org/10.1016/j.actamat.2022.117781.

[32] T. Gustmann, F. Gutmann, F. Wenz, P. Koch, R. Stelzer, W.G. Drossel, H. Korn, Properties of a superelastic NiTi shape memory alloy using laser powder bed fusion and adaptive scanning strategies, Prog. Addit. Manuf. 5 (2020) 11–18, https://doi.org/10.1007/s40964-020-00118-6.

[33] Z. Gorgin Karaji, M. Speirs, S. Dadbakhsh, J.P. Kruth, H. Weinans, A.A. Zadpoor, S. A. Yavari, Additively manufactured and surface biofunctionalized porous nitinol, ACS Appl. Mater. Interfaces 9 (2017) 1293–1304, https://doi.org/10.1021/acsami.6b14026.

[34] P. Jamshidi, C. Panwisawas, E. Langi, S.C. Cox, J. Feng, L. Zhao, M.M. Attallah, Development, characterisation, and modelling of processability of nitinol stents using laser powder bed fusion, J. Alloy. Compd. 909 (2022), 164681, https://doi.org/10.1016/j.jallcom.2022.164681.

[35] C. Tan, J. Zou, S. Li, P. Jamshidi, A. Abena, A. Forsey, R.J. Moat, K. Essa, M. Wang, K. Zhou, M.M. Attallah, Additive manufacturing of bio-inspired multi-scale hierarchically strengthened lattice structures, Int. J. Mach. Tools Manuf. 167 (2021), 103764, https://doi.org/10.1016/j.ijmachtools.2021.103764.

[36] Z. Xiong, H. Li, H. Yang, Y. Yang, Y. Liu, L. Cui, X. Li, Micro laser powder bed fusion of NiTi alloys with superior mechanical property and shape recovery function, Addit. Manuf. 57 (2022), 102960, https://doi.org/10.1016/j.addma.2022.102960.

[37] S. Saedi, S.E. Saghaian, A. Jahadakbar, N. Shayesteh Moghaddam, M. Taheri Andani, S.M. Saghaian, Y.C. Lu, M. Elahinia, H.E. Karaca, Shape memory response of porous NiTi shape memory alloys fabricated by selective laser melting, J. Mater. Sci. Mater. Med. 29 (2018), https://doi.org/10.1007/s10856-018-6044-6.

[38] X. Yang, Q. Yang, Y. Shi, L. Yang, S. Wu, C. Yan, Y. Shi, Effect of volume fraction and unit cell size on manufacturability and compressive behaviors of Ni-Ti triply periodic minimal surface lattices, Addit. Manuf. 54 (2022), 102737, https://doi.org/10.1016/j.addma.2022.102737.

[39] C. Cisse, W. Zaki, T. Ben Zineb, A review of constitutive models and modeling techniques for shape memory alloys, Int. J. Plast. 76 (2016) 244–284, https://doi.org/10.1016/j.ijplas.2015.08.006.

[40] C.M. Portela, J.R. Greer, D.M. Kochmann, Impact of node geometry on the effective stiffness of non-slender three-dimensional truss lattice architectures, Extrem. Mech. Lett. 22 (2018) 138–148, https://doi.org/10.1016/j.eml.2018.06.004.

[41] F. Auricchio, R.L. Taylor, J. Lubiner, Computer methods in applied mechanics and engineering Shape-memory alloys: macromodelling and numerical simulations of the superelastic behavior, Comput. Methods Appl. Mech. Eng. 146 (1997) 281–312, https://doi.org/10.1016/S0045-7825(96)01232-7.

[42] S. Saedi, A.S. Turabi, M.T. Andani, C. Haberland, H. Karaca, M. Elahinia, The influence of heat treatment on the thermomechanical response of Ni-rich NiTi alloys manufactured by selective laser melting, J. Alloy. Compd. 677 (2016) 204–210, https://doi.org/10.1016/j.jallcom.2016.03.161.

[43] P. Šittner, L. Heller, J. Pilch, C. Curfs, T. Alonso, D. Favier, Young's modulus of austenite and martensite phases in superelastic NiTi wires, J. Mater. Eng. Perform. 23 (2014) 2303–2314, https://doi.org/10.1007/s11665-014-0976-x.

[44] P. Šittner, M. Landa, P. Lukáš, V. Novák, R-phase transformation phenomena in thermomechanically loaded NiTi polycrystals, Mech. Mater. 38 (2006) 475–492, https://doi.org/10.1016/j.mechmat.2005.05.025.

[45] G. Machado, H. Louche, T. Alonso, D. Favier, Superelastic cellular NiTi tube-based materials: fabrication, experiments and modeling, Mater. Des. 65 (2015) 212–220, https://doi.org/10.1016/j.matdes.2014.09.007.

[46] D. Garoz, F.A. Gilabert, R.D.B. Sevenois, S.W.F. Spronk, W. Van Paepegem, Consistent application of periodic boundary conditions in implicit and explicit finite element simulations of damage in composites, Compos. Part B Eng. 168 (2019) 254–266, https://doi.org/10.1016/j.compositesb.2018.12.023.

[47] W. Wu, J. Owino, A. Al-Ostaz, L. Cai, Applying periodic boundary conditions in finite element analysis, In: Proceedings of the SIMULIA Community Conf. Provid., 2014: pp. 707–719.

[48] E. Borisov, K. Starikov, A. Popovich, T. Tihonovskaya, Investigation of the possibility of tailoring the chemical composition of the NiTi alloy by selective laser melting, Metals 11 (2021) 1–11, https://doi.org/10.3390/met11091470.

[49] X. Cao, Y. Jiang, T. Zhao, P. Wang, Y. Wang, Z. Chen, Y. Li, D. Xiao, D. Fang, Compression experiment and numerical evaluation on mechanical responses of the lattice structures with stochastic geometric defects originated from additive-manufacturing, Compos. Part B Eng. 194 (2020), 108030, https://doi.org/10.1016/j.compositesb.2020.108030.

[50] T. DebRoy, H.L. Wei, J.S. Zuback, T. Mukherjee, J.W. Elmer, J.O. Milewski, A. M. Beese, A. Wilson-Heid, A. De, W. Zhang, Additive manufacturing of metallic

components – process, structure and properties, Prog. Mater. Sci. 92 (2018) 112–224, https://doi.org/10.1016/j.pmatsci.2017.10.001.

[51] S.N. Khaderi, V.S. Deshpande, N.A. Fleck, The stiffness and strength of the gyroid lattice, Int. J. Solids Struct. 51 (2014) 3866–3877, https://doi.org/10.1016/j.ijsolstr.2014.06.024.

[52] J. Zhang, R.J. Perez, E.J. Lavernia, Documentation of damping capacity of metallic, ceramic and metal-matrix composite materials, J. Mater. Sci. 28 (1993) 2395–2404, https://doi.org/10.1007/BF01151671.

[53] J. Zhang, H. Huang, G. Liu, H. Zong, C. Zhang, Stiffness and energy absorption of additive manufactured hybrid lattice structures, Virtual Phys. Prototyp. 16 (2021) 428–443, https://doi.org/10.1080/17452759.2021.1954405.

[54] J.P. Oliveira, R.M. Miranda, F.M.Braz Fernandes, Welding and joining of NiTi shape memory alloys: a review, Prog. Mater. Sci. 88 (2017) 412–466, https://doi.org/10.1016/j.pmatsci.2017.04.008.

[55] K. Ushijima, W.J. Cantwell, R.A.W. Mines, S. Tsopanos, M. Smith, An investigation into the compressive properties of stainless steel micro-lattice structures, J. Sandw. Struct. Mater. 13 (2011) 303–329, https://doi.org/10.1177/1099636210380997.

[56] S.K. S, I.A. Kumar, L. Marandi, I. Sen, Assessment of small-scale deformation characteristics and stress-strain behavior of NiTi based shape memory alloy using nanoindentation, Acta Mater. 201 (2020) 303–315, https://doi.org/10.1016/j.actamat.2020.09.080.

[57] W.C. Oliver, G.M. Pharr, Measurement of hardness and elastic modulus by instrumented indentation: advances in understanding and refinements to methodology, J. Mater. Res. 19 (2004) 3–20, https://doi.org/10.1557/jmr.2004.19.1.3.

[58] Y. Zhang, Y.T. Cheng, D.S. Grummon, Finite element modeling of indentation-induced superelastic effect using a three-dimensional constitutive model for shape memory materials with plasticity, J. Appl. Phys. 101 (2007), https://doi.org/10.1063/1.2436928.